Advanced Powder Materials 3 (2024) 100168

Contents lists available at ScienceDirect

Advanced Powder Materials

journal homepage: www.keaipublishing.com/en/journals/advanced-powder-materials

Insight into the effect of Ti substitutions on the static oxidation behavior of (Hf,Ti)C at 2500 °C

Shiyan Chen [a], Zhaoke Chen [a,*], Jinming Wang [b], Yi Zeng [a], Weilong Song [a], Xiang Xiong [a,**], Xingchao Li [b], Tongqi Li [b], Yichen Wang [a]

[a] State Key Laboratory of Powder Metallurgy, Central South University, Changsha 410083, China
[b] Aerospace Research Institute of Materials & Processing Technology, China Academy of Launch Vehicle Technology, Beijing 100076, China

ARTICLE INFO

Keywords:
Ultra-high temperature ceramics (UHTCs)
(Hf
Ti)C
Static oxidation behavior
Hf-based carbides
Oxidation mechanism

ABSTRACT

Hf-based carbides are highly desirable candidate materials for oxidizing environments above 2000 °C. However, the static oxidation behavior at their potential service temperatures remains unclear. To fill this gap, the static oxidation behavior of (Hf, Ti)C and the effect of Ti substitutions were investigated in air at 2500 °C under an oxygen partial pressure of 4.2 kPa. After oxidation for 2000 s, the thickness of the oxide layer on the surface of (Hf, Ti)C bulk ceramic is reduced by 62.29 % compared with that on the HfC monocarbide surface. The dramatic improvement in oxidation resistance is attributed to the unique oxide layer structure consisting of various crystalline oxycarbides, HfO_2, and carbon. The Ti-rich oxycarbide ((Ti, Hf)C_xO_y) dispersed within HfO_2 formed the major structure of the oxide layer. A coherent boundary with lattice distortion existed at the HfO_2/(Ti, Hf)C_xO_y interface along the (111) crystal plane direction, which served as an effective oxygen diffusion barrier. The Hf-rich oxycarbide ((Hf, Ti)C_xO_y) together with (Ti, Hf)C_xO_y, HfO_2, and precipitated carbon constituted a dense transition layer, ensuring favorable bonding between the oxide layer and the matrix. The Ti content affects the oxidation resistance of (Hf, Ti)C by determining the oxide layer's phase distribution and integrity.

1. Introduction

Ultra-high temperature ceramics (UHTCs) are considered as the most promising candidates for a new generation of thermal protection materials (TPMs) [1,2]. Among the UHTCs, HfC receives considerable attention due to its extremely high melting point (~3830 °C), favorable elastic modulus, and high hardness at elevated temperatures [3]. The attractive properties offer HfC and Hf-based carbides great potential for applications in extreme environments above 2000 °C, especially in aerospace TPMs [4,5]. However, the deficient oxidation resistance of HfC limits its application [6]. Glechner et al. [7] reported that the onset oxidation temperature (OOT) of HfC was only 550 °C. Shimada et al. [8] observed numerous cracks in the HfO_2 layer formed by oxidation of HfC at 600–800 °C. Scott et al. [9] demonstrated that the surface of HfC was covered by a porous HfO_2 layer after oxidation at 1300 °C, which is unable to provide effective protection. Similar experimental findings were identified by Bargeron et al. [10] and Berkowitz et al. [11].

Adding group IV-V elements (e.g., Ti and Ta) to form a solid solution is a practical and effective approach for enhancing the oxidation resistance of carbides [12–16]. Zhang et al. [17] demonstrated that the oxidation resistance of (Hf, Ta)C is significantly enhanced compared to HfC at 1400–1600 °C due to the formation of the compact oxygen barriers. Lun et al. [18] found that substituting Ti for Zr in (Zr, Ti)C_x facilitates the formation of a dense Zr–Ti–C–O layer and raises the onset oxidation temperature. Furthermore, Backman et al. [19] reported that the group IV oxides were the most thermodynamically stable, which might promote the establishment of an effective protective layer. Thus, it is reasonable to infer that adding Ti could provide a more significant enhancement of the oxidation resistance of HfC, despite the effect of Ti addition on the oxidation resistance of HfC remains unclear.

Static oxidation testing serves as an effective method for investigating the intrinsic oxidation resistance of Hf-based carbides, which forms a critical foundation for the compositional selection and design of TPMs. Although ablation testing provides a good simulation of the operating conditions of Hf-based carbides [20–22], it encompasses both physical (e.g., airflow scouring) and chemical factors (e.g., corrosive oxidation)

* Corresponding author.
** Corresponding author.
E-mail addresses: chenzhaoke2008@csu.edu.cn (Z. Chen), xiongx@csu.edu.cn (X. Xiong).

https://doi.org/10.1016/j.apmate.2023.100168
Received 17 August 2023; Received in revised form 14 November 2023; Accepted 15 November 2023
Available online 3 December 2023
2772-834X/© 2023 Central South University. Publishing services by Elsevier B.V. on behalf of KeAi Communications Co. Ltd. This is an open access article under the CC BY-NC-ND license (http://creativecommons.org/licenses/by-nc-nd/4.0/).

[23–26]. The comprehensive effects lead to substantial damage to the oxide layer during ablation, posing challenges for in-depth analysis of the influence of oxidation on the material's performance. In contrast, static oxidation testing minimizes the impact of physical factors, allowing the formation of a more complete oxide layer [27]. This preservation of structural information provides a clear understanding of the material's inherent oxidation behavior. The investigation of the static oxidation behavior aims to unveil the intrinsic oxidation resistance of Hf-based carbides from the perspective of materials science, elucidating the effect of chemical oxidation on their practical performance. Consequently, understanding the static oxidation behavior of Hf-based carbides holds significance in composition optimization and performance improvement of TPMs. Furthermore, static oxidation tests can extend over longer durations than ablation tests, enabling a more comprehensive and complete evaluation of the material's long-term oxidation resistance. Also, it can help explore the potential of Hf-based carbides for other high-temperature applications.

Efforts have been dedicated to investigating the static oxidation behaviors of Hf-based carbides [28–32]. Opeka et al. [33] suggested that the ideal protective layer should be a multi-oxide scale, in which high-melting-point oxides form the skeleton and low-melting-point oxides serve as the filler phase. Similar structures have been observed in various Hf-based carbide systems, such as Hf–Si–C system reported by Wen [34], Hf–Al–C system reported by Gaydaychuk [35], and Hf–Ta–C system reported by Pienti [36]. Unfortunately, the challenge lies in the fact that present studies on the static oxidation behaviors of Hf-based carbides have primarily focused on temperatures below 1600 °C, with minimal research above 2000 °C (Fig. S1). In fact, the potential service temperatures for Hf-based carbides are far exceed 1600 °C, even reaching 2000 °C or higher. The oxidation mechanisms established at low temperatures may not thoroughly elucidate the oxidation behaviors at ultra-high temperature due to the possibility of evaporation and decomposition of oxidation products [37]. Therefore, it is urgent to fill this gap by investigating the static oxidation behaviors of Hf-based carbides at their potential service temperatures (above 2000 °C) [38–40].

In this study, the static oxidation behaviors of (Hf, Ti)C bulk ceramics were investigated at 2500 °C, as well as the effect of Ti substitutions on the oxidation resistance of the solid solutions. The comprehensive microstructure characterization of the oxide layer was reported. Moreover, the oxidation mechanism was discussed in detail, which could contribute to the composition optimization of UHTCs and expand their applications at ultra-high temperatures.

2. Results and discussion

2.1. Phase composition and microstructure of initial samples

Fig. 1a and b shows XRD patterns of (Hf, Ti)C. The XRD analysis reveals that all samples exhibit only one set of diffraction peaks, indicating the formation of a single-phase face-centered cubic (FCC) structure. Fig. 1b shows all the peaks shift slightly to the right, i.e., toward to higher 2θ angles, with increasing Ti content. This lattice shrinkage can be attributed to the substitution of Ti atoms (atomic radius: 140 p.m.), which are smaller than Hf atoms (atomic radius: 155 p.m.) [41]. Fig. 1c to f displays dense microstructures of (Hf, Ti)C, consistent with the relative densities measured for samples above 95 %. The EDS mappings (Fig. 1g) reveal a uniform distribution of Hf, Ti, and C elements, indicating significant compositional homogeneity within the (Hf, Ti)C samples.

2.2. Oxidation kinetics

The microscopic morphology of HT0 to HT3 before and after oxidation is illustrated in Fig. 2a. The initial samples exhibit a smooth and mirror-like surface without cracks or pores. After oxidation at 2500 °C, numerous bubbles appeared randomly on the surface of the (Hf, Ti)C. The

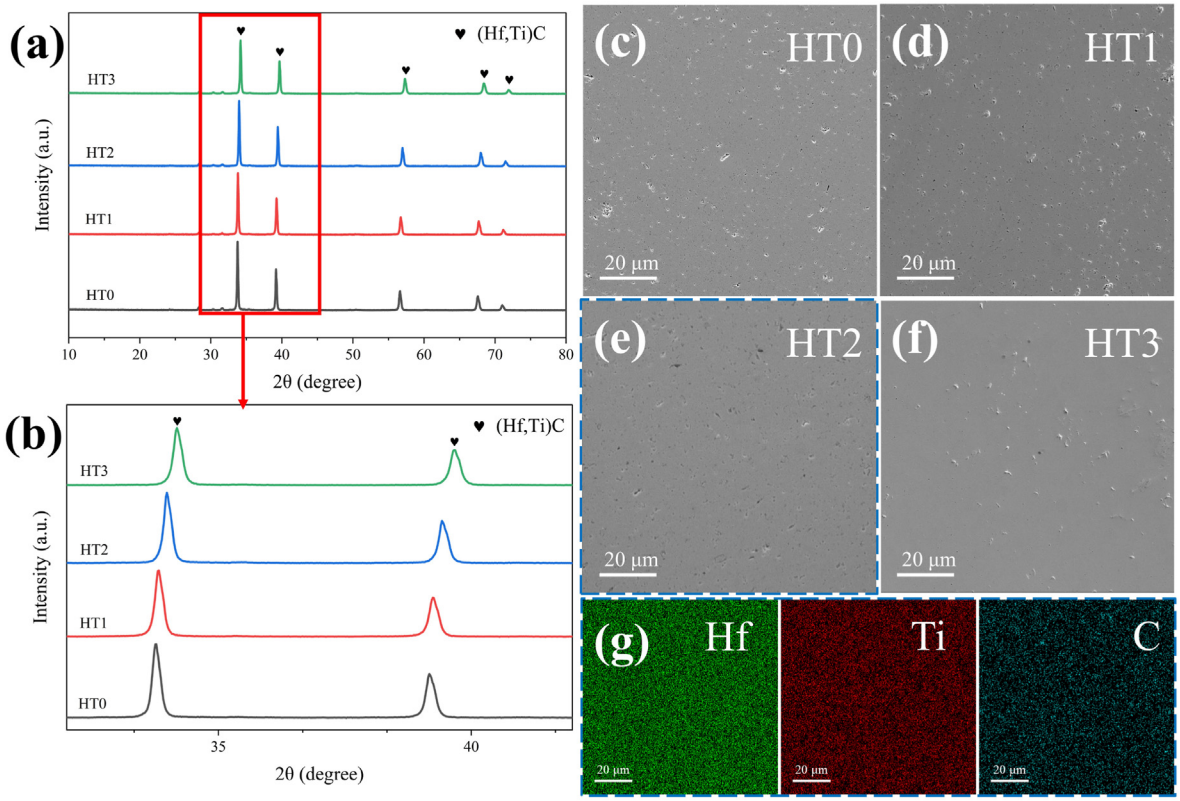

Fig. 1. XRD patterns and SEM images of (Hf, Ti)C samples. (a) XRD patterns; (b) Enlarged XRD patterns from 32° to 42°; (c)–(f) SEM images of HT0 (c), HT1 (d), HT2 (e), and HT3 (f); (g) Elemental mappings of HT2.

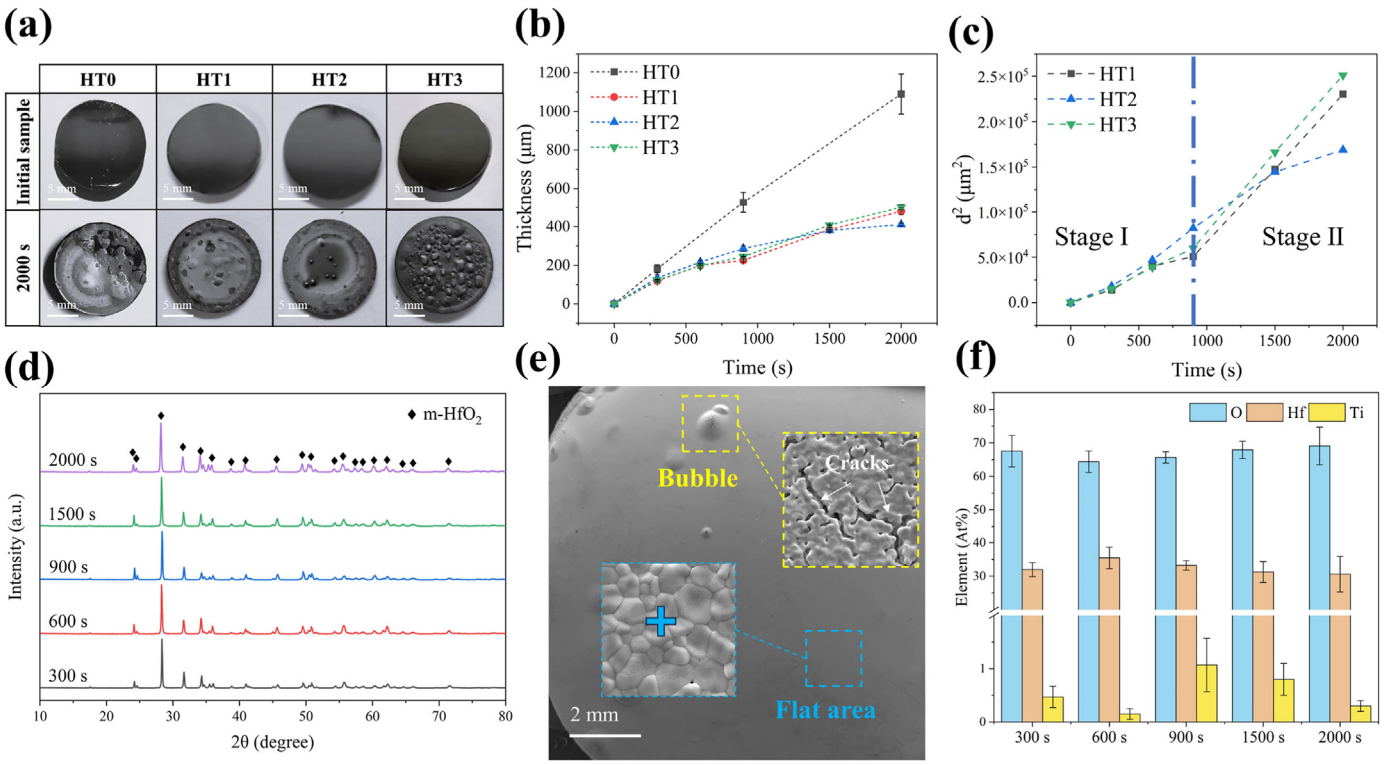

Fig. 2. Surface structure and oxidation kinetics analysis of HT0-HT3 after oxidation at 2500 °C. (a) Morphology of HT0-HT3 before and after oxidation; (b) The oxide layer thickness of oxidized samples as a function of oxidation time; (c) The square of the oxide layer thickness of oxidized samples as a function of oxidation time; (d) XRD patterns of HT2 surface after oxidation; (e) Surface microstructure of HT2-900; (f) EDS results of points in the flat areas of HT2 surface.

number of bubbles on the oxidized surface initially decreases but increases as the Ti content rises. HT2 exhibits the fewest bubbles after oxidation, implying a promising structural stability at ultra-high temperatures.

The thickness of the oxide layer is an applicable indicator of the oxidation resistance of the material. The specimens were cut along the diameter after oxidation at 2500 °C, and the morphology of the oxide layer's central region was observed using SEM. The oxide layer's thickness was measured by calculating the average of several locations. As shown in Fig. 2b, the oxide layer thickness of all samples increases with oxidation time extend, but only HT0 show a liner increase. The samples with Ti doping show a much thinner oxide layer than pure HfC, suggesting a reduced oxidation rate and enhanced oxidation resistance. The cross-sectional micromorphology of HT0 after oxidation at 2500 °C for 2000 s (HT0-2000) is shown in Fig. S2. The thickness of the oxide layer on the HT0's surface is measured to be 1090 μm. Innumerable cracks and pores are observed in the oxide layer, as reported in previous studies [8–10]. Compared to HT0, the oxide layer thickness of HT2-2000 (411 μm) is reduced by 62.29%, demonstrating that the (Hf, Ti)C showing a better oxidation resistance than pure HfC.

The Ti-doped samples (HT1-HT3) exhibit similar oxidation behavior. The relationship between the square of the oxide layer thickness (d) and the oxidation time is depicted in Fig. 2c. According to the fitting results, the oxidation process of HT1-HT3 can be divided into two stages: Stage I before 900 s and Stage II after 900 s. A linear correlation between d^2 and the oxidation time in both stages was observed, revealing that the oxidation process of HT1-HT3 was controlled by diffusion mechanisms and follows a two-stage parabolic law [42–44]. This behavior can be described by Equation (1):

$$(d - d_0)^2 = kt \quad (1)$$

where d_0 is the initial oxide layer thickness, t is the oxidation time, d is the oxide layer thickness after oxidation, and k refers to the oxidation rate constant.

The k values of HT1-HT3 at different stages are illustrated in Table 1. With an increase of Ti content, k_1 (the k value of Stage I) initially increases and then decreases. However, the k_2 (the k value of Stage II) shows the opposite trend. The k_2 of HT1 and HT3 increases dramatically, suggesting that HT1 and HT3 suffered more intense oxidation during Stage II. In contrast, HT2 exhibits the lowest k_2, which is even lower than k_1. As a result, HT2 possesses the thinnest oxide layer after 2000 s of oxidation, demonstrating better long-term oxidation resistance.

2.3. Structural evolution of (Hf, Ti)C during oxidation

2.3.1. Microstructure and phase composition of surface

Microstructure analysis of the oxide layer on (Hf, Ti)C surface was performed using HT2 as an example due to its superior long-term oxidation resistance, as indicated by the kinetic results. The XRD patterns of the HT2 surface after oxidation at 2500 °C are shown in Fig. 2d. After 300 s of oxidation, carbides were not detectable on the HT2's surface, and the oxides were completely covered all samples. Only monoclinic HfO_2 (m-HfO_2) was observed on the surface of the HT2, while Ti-containing phases were absent. There are three possible reasons for the absence of Ti-containing oxides in XRD patterns. Firstly, Ti-containing oxides might form solid solutions with HfO_2 at 2500 °C but their negligible amount are not detectable. Secondly, the molten Ti-containing oxides might flow and fill the pores in the inner oxide layer due to their relatively low melting point (e.g., TiO_2, 1912 °C) [45]. Finally, the

Table 1
Summary of k values for HT1–HT3.

Composition	k (μm²/s)	
	Stage I (k_1)	Stage II (k_2)
HT1	59.53	163.14
HT2	91.60	79.83
HT3	67.83	173.92

Ti-containing oxides might evaporate significantly during oxidation and slightly during subsequent fast cooling at extremely high temperatures [46,47]. Fig. S3 demonstrates the XRD patterns of the surface of HT1 and HT3 after oxidation at 2500 °C for different oxidation time. The phase composition of the (Hf, Ti)C surface after oxidation remains m-HfO_2, regardless of variations in Ti content.

The oxidized surface of HT2 displays distinct features, including flat areas and bubbles (Fig. 2e). The flat areas consist of irregular oxide grains arranged closely. In comparison, the bubbles exhibit numerous cracks resulting from the release of gaseous products. The surface microstructures of the flat areas in HT2 after oxidation for different oxidation time are shown in Fig. S4. With increasing oxidation time, the grains within the flat areas experience significant growth, as the average grain size increases from 3.18 ± 1.07 μm (HT2-300) to 7.22 ± 2.78 μm (HT2-2000). The EDS results (Fig. 2f) confirm that the primary composition of the oxidized surface is HfO_2, with minimal Ti content (≤2 at%), which is consistent with the XRD findings.

2.3.2. *Microstructure and phase composition of cross-section*

The HT2-900 (the turning point between Stage I and Stage II) was chosen as a representative specimen for an in-depth analysis of the microstructural evolution during oxidation. Fig. 3a illustrates the elemental distribution in the HT2-900 cross-section. The oxygen distribution indicates a uniform oxide layer thickness, suggesting that the surface of HT2-900 experienced an analogous degree of oxidation. A distinct Hf-rich layer is observed in the outermost oxide layer, consistent with the EDS results in Fig. 2f. Interestingly, Ti exhibits a noticeable aggregation within the oxide layer, with a distinct Ti-rich layer observed. The Hf and O contents are relatively low in the Ti-rich layer. Additionally, numerous Ti-rich particles are dispersed in the oxide layer.

Fig. 3b depicts the magnified morphology of the oxide layer in HT2-900. The oxide layer exhibits an excellent adhesion with the carbide matrix without cracks or voids. Moreover, a distinct layered structure is observed within the oxide layer. The oxide layer can be divided into four layers based on the different regions' elemental distribution and unique microstructural characteristics.

The outermost layer (Layer I) is a continuous HfO_2 layer (Fig. 3c), which contains numerous micro-pores resulting from the release of gaseous products. The second layer (Layer II) corresponds to the Ti-rich layer as shown in Fig. 3a. The white contrast in this layer represents HfO_2, while the dark contrast denotes the Ti-rich phase and follows the higher Ti/Hf ratio the darker (Spot 2, Fig. 3g). The Ti-rich phase is embedded within the HfO_2, forming a compact HfO_2 + Ti-rich phase structure (Fig. 3d). Layer III displays a porous structure consisting of HfO_2 and a Ti-rich phase, as shown in Fig. 3e. However, the Ti-rich phase within Layer III is smaller and fewer than that in Layer II. Layer III and Layer II constitute the major structure of the oxide layer. Lastly, Layer IV represents the transition layer between the oxide layer and the carbide substrate (Fig. 3f), consisting of carbon, Ti-rich phases, and HfO_2 (Spots 4–5, Fig. 3g). Carbon precipitation is observed between the Ti-rich phase and HfO_2, forming a HfO_2 + Ti-rich phase + C structure. This structure ensures a strong bonding between the oxide layer and the substrate. Fig. S5 depicts the microstructure of the oxide layer in HT2-2000. The proportion of the Ti-rich phase increases in Layer IV with increasing oxidation time. Furthermore, the microstructural features of the oxide layer in HT2-2000 show no significant changes. These findings illustrate that the microstructure of the oxide layer in HT2 remains stable during the oxidation progress.

2.3.3. *Initial oxide layer-transition layer*

The microstructure of the transition layer between the oxide layer and the carbide matrix might reveal the structural evolution and oxidation mechanism during the initial oxidation stage. As depicted in Fig. 4a, a thin film was extracted from the transition layer (Layer IV, Fig. 3f) in

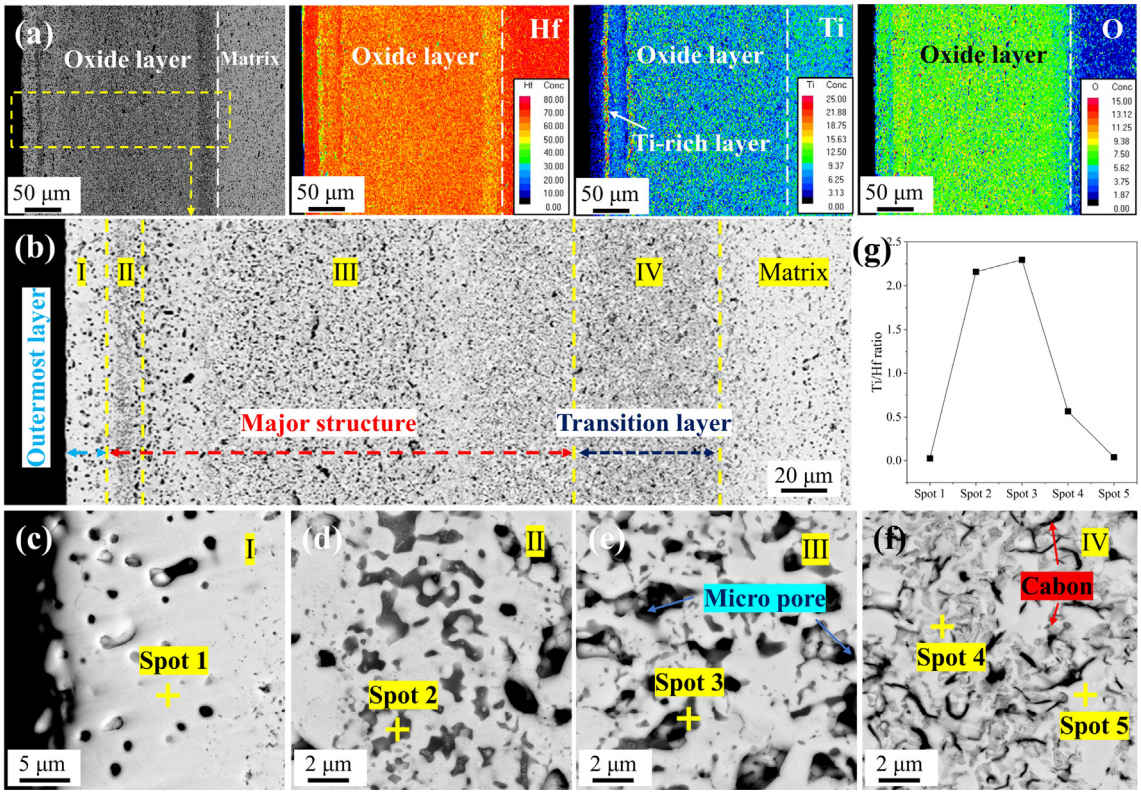

Fig. 3. Cross-sectional microstructure analysis of the oxide layer in HT2-900. (a) SEM image and elemental mappings of the oxide layer; (b) Magnified SEM image of the oxide layer; (c) SEM image of Layer I; (d) SEM image of Layer II; (e) SEM image of Layer III; (f) SEM image of Layer IV; (g) Ratio of metal element content of Spots 1–5.

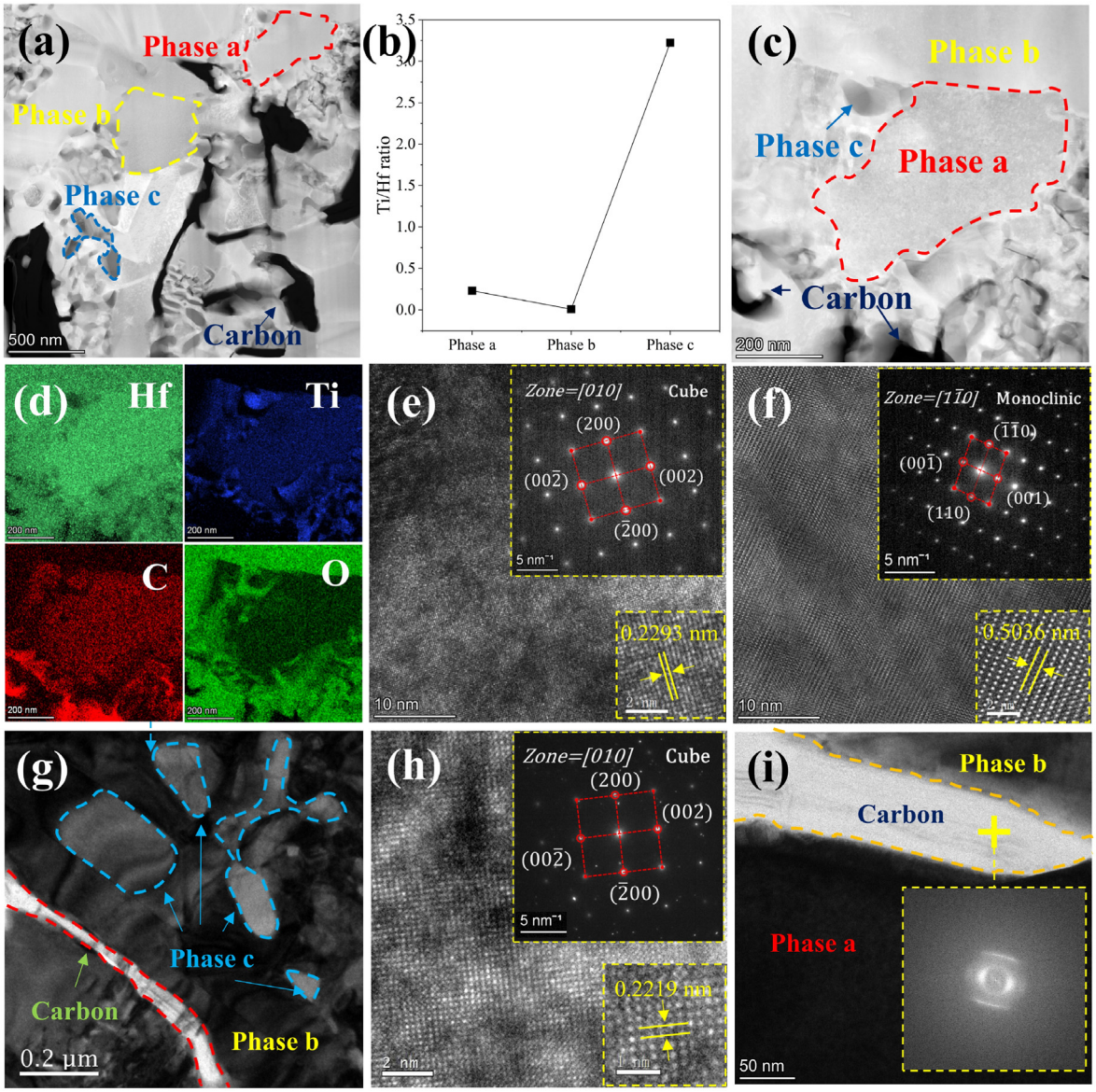

Fig. 4. Microstructure analysis of transition layer in HT2-900. (a) HAADF-STEM image of the transition layer; (b) Ratio between Ti and Hf in Phase a, Phase b, and Phase c; (c) Magnified HAADF-STEM view of the transition layer; (d) STEM-EDS elemental mappings of (c); (e) HRTEM image of Phase a with corresponding SAED pattern inset; (f) HRTEM image of Phase b with corresponding SAED pattern inset; (g) TEM image of Phase c cluster; (h) HRTEM image of Phase c with corresponding SAED pattern inset; (i) HRTEM image of precipitated carbon with corresponding FFT pattern inset.

HT2-900 using FIB technology. From the EDS results (Fig. 4b) and the high-angle annular dark field (HAADF) images (Fig. 4c), the transition layer is composed of three phases along with carbon precipitation: Phase a, characterized by Hf enrichment and Ti deficiency; Phase b, almost devoid of Ti; and Phase c, exhibiting Ti enrichment and Hf deficiency. Carbon precipitation could also be observed between the phases. The phases within the transition layer exhibit excellent interfacial bonding, and the transition layer is devoid of any microcracks or micropores, which agrees with the dense microstructure observed via SEM.

The elemental distribution in the localized region (Fig. 4d) confirms the presence of Hf, Ti, O, and C within Phase a; hence, it is designated as the (Hf, Ti)C_xO_y phase. The elements with higher content will be mentioned first in the name (e.g., the elemental content in (Hf, Ti)C_xO_y: Hf > Ti, C > O) to simplify the description. Notably, the high-resolution transmission electron microscope (HRTEM) image and selected area electron diffraction (SAED) pattern (Fig. 4e) reveal a shared crystal structure between the (Hf, Ti)C_xO_y phase and HT2. The (Hf, Ti)C_xO_y phase exhibits an FCC structure with a lattice spacing of 0.2293 nm along the (002) crystal plane. This lattice spacing value (0.2293 nm) lies between the lattice spacings of TiC (PDF# 01-075-6426, 0.2145 nm) and HfC (PDF# 00-039-1491, 0.2319 nm). Prior research substantiated that transition metal carbides can dissolve a certain quantity of oxygen [48]. Therefore, it can be inferred that the formation of the (Hf, Ti)C_xO_y phase occurs during the initial stages of oxidation, involving the dissolution of a few oxygen atoms into the HT2 lattice. The (Hf, Ti)C_xO_y phase retains the same FCC structure as HT2 until the dissolved oxygen content within the HT2 lattice reaches its maximum solubility.

Based on the HRTEM image and the SAED pattern (Fig. 4f), Phase b is identified as m-HfO_2. The (001) interplanar spacing of Phase b is measured to be 0.5036 nm, which closely matches the reference value of m-HfO_2 (PDF# 04-008-4635, 0.5030 nm). Additionally, Phase c is discovered adjacent to the m-HfO_2 grains. But Phase c grains are smaller than Phase a and b (Fig. 4g). As calibrated by the SAED pattern (Fig. 4h), Phase c possesses an FCC structure with a (200) interplanar spacing of 0.2219 nm, slightly larger than the reference value of TiC (PDF# 01-075-6426, 0.2145 nm). Phase c and Phase a share the same crystal structure.

However, Phase c shows a higher Ti and lower O content than Phase a, thus designating it as the (Ti, Hf)C_xO_y-L phase. In other words, the structure of the (Ti, Hf)C_xO_y-L is equivalent to the dissolution of a few Hf and O atoms into the TiC lattice. Interestingly, the Phase c with fine grains size is commonly enclosed by Phase b (m-HfO_2), making its detection challenging under SEM (Fig. 3). Phase b is characterized as a Hf-rich phase, while Phase c represents a Ti-rich phase, suggesting that they resemble the decomposition products of Phase a. The presence of carbon distributed among different phases indicates the occurrence of carbon precipitation during the oxidation process, as depicted in Fig. 4i. Therefore, it can be seen that the transition layer comprises (Hf, Ti)C_xO_y (Phase a), HfO_2 (Phase b), (Ti, Hf)C_xO_y-L (Phase c) and carbon.

2.3.4. *Major structure of the oxide layer - HfO_2+(Ti,Hf)C_xO_y-H*

The previous characterization results indicate that the major structure of the oxide layer, i.e., layer II (Fig. 3d) and layer III (Fig. 3e), are originated from the further oxidation of the transition layer. To further disclose the oxidation behavior and mechanism, a thin film specimen (Fig. 5a) was extracted from the major structure of the oxide layer in the HT2-900 sample (Fig. 3b). The TEM image (Fig. 5a) and the corresponding EDS results (Fig. 5e) reveal that the major structure of the oxide layer comprises granular Phase d and elongated Phase e. Phase d predominantly consists of Hf and O elements. According to the HRTEM image and SAED pattern (Fig. 5b), Phase d is identified as m-HfO_2 with a (001) plane spacing of 0.5005 nm, which is slightly lower than that of Phase b in the transition layer. This discrepancy arises from the diffusion of trace Ti atoms into the lattice of Phase b during further oxidation and replacing larger Hf atoms, consistent with the EDS results (Fig. 3g). Phase e was calibrated to be the same FCC structure as Phase c. Still, with a (002) interplanar spacing of 0.2106 nm, slightly smaller than that of Phase c in the transition layer (Fig. 5d). This decrease is attributed to the continuous inward diffusion of oxygen during oxidation, leading to the dissolution of a few O atoms (atomic radius: 48 p.m.) into the Phase c lattice and replacing C atoms (atomic radius: 67 p.m.). Consequently, Phase e exhibits a higher O content than Phase c and is denoted as the (Ti, Hf)C_xO_y-H phase.

Moreover, Fig. 5f to g illustrate the presence of a transitional region measuring approximately 60 nm at the interface between HfO_2 (Phase d)

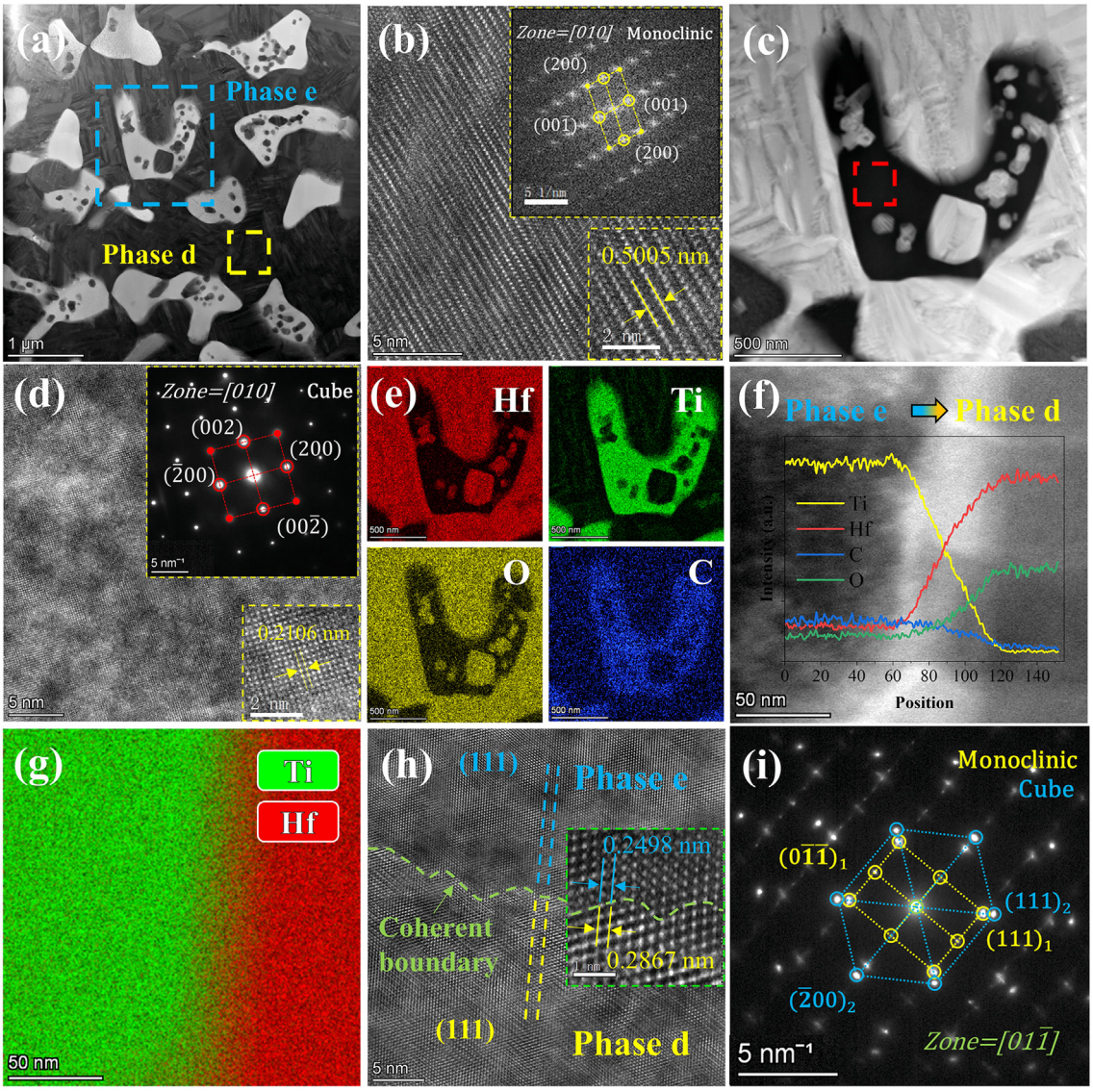

Fig. 5. Microstructure analysis of the major structure of the oxide layer in HT2-900. (a) TEM image of the major structure of the oxide layer; (b) HRTEM image of Phase d with corresponding FFT pattern inset; (c) Magnified HAADF-STEM view of Phase e; (d) HRTEM image of Phase e with corresponding SAED pattern inset; (e) STEM-EDS elemental mappings of (c); (f) TEM image and STEM-EDS line scan of the Phase d/Phase e interface; (g) STEM-EDS elemental mappings of Hf and Ti in (i); (h) HRTEM image of the Phase d/Phase e interface, (i) SAED pattern of the Phase d/Phase e interface.

and (Ti, Hf)C_xO_y-H (Phase e). Notably, the HRTEM image and SAED pattern of the HfO_2/(Ti, Hf)C_xO_y-H interface reveal a coherent relationship between HfO_2 (monoclinic structure) and (Ti, Hf)C_xO_y-H (cubic structure) in the (111) crystal plane direction (Fig. 5h–i). The (111) interplanar spacing of (Ti, Hf)C_xO_y-H is measured to be 0.2483 nm, whereas for HfO_2, it is 0.2867 nm. Despite the lattice interconnection of the two phases can establish a coherent phase boundary between HfO_2 and (Ti, Hf)C_xO_y-H, there is severe lattice distortion at the HfO_2/(Ti, Hf)C_xO_y-H interface, due to the disparities in interplanar spacing and crystal structure. Therefore, the interface has a sluggish diffusion effect, effectively preventing oxygen's inward diffusion [48–51].

Fig. 5c reveals the presence of particle clusters within Phase e ((Ti, Hf)C_xO_y-H). The microstructure of the particles is shown in Fig. S6. According to the EDS results and the SAED pattern, these particles were identified as Phase d (m-HfO_2). Similarly, the HRTEM image and the corresponding fast Fourier transformation (FFT) image indicate a coherent phase boundary between Phase e and the internal Phase d particles along the (111) crystal plane direction (Fig. S6b). The coherent relationship and the smooth compositional transition between Phase d and Phase e provide a natural barrier to impede the oxygen diffusion. The microstructure and composition of layer III are identical to those of layer II, except that the (Ti, Hf)C_xO_y-H particles in layer III are smaller and lower in content. Generally, the major structure of the oxide layer consists of HfO_2 (Phase d) and (Ti, Hf)C_xO_y-H (Phase e).

2.4. Oxidation mechanism

Without taking the solid solution effect into account, which assumes HfC and TiC exist as individual phases, the oxidation process can be described by the following reactions:

$$HfC_{(s)} + 1.5O_{2(g)} \rightarrow HfO_{2(s)} + CO_{(g)} \quad (2)$$

$$TiC_{(s)} + 1.5O_{2(g)} \rightarrow TiO_{2(l)} + CO_{(g)} \quad (3)$$

$$TiC_{(s)} + O_{2(g)} \rightarrow TiO_{(l)} + CO_{(g)} \quad (4)$$

$$CO_{(g)} + 0.5O_{2(g)} \rightarrow CO_{2(g)} \quad (5)$$

Fig. S7 illustrates the Ellingham diagram for the Hf–Ti–C–O system and the volatility diagrams for HfC and TiC at 2500 °C. As mentioned above, the Gibbs free energy (ΔG) of the reactions at the test temperature is negative, signifying their spontaneous progress. Notably, the ΔG value for the oxidation reaction of HfC is lower than that of TiC, suggesting a higher tendency of HfC to oxidize in the test temperature range. The oxide layer on the surface of (Hf, Ti)C bulk effectively hinders the inward diffusion of oxygen, resulting in a gradual decrease in the oxygen partial pressure from the surface to the interior of the oxide layer. The oxygen partial pressure reaches the lowest value at the interface between the oxide layer and the substrate. Under this low oxygen partial pressures level, there is insufficient oxygen to react with carbides, leading to a competitive oxidation mechanism between HfC and TiC.

Volatility diagrams illustrate the relationship between the vapor pressure of the predominant gaseous species and the equilibrium partial pressures of O_2 (pO_2) at designed temperatures. According to the calculated volatility diagrams of HfC and TiC (Figs. S7b–c), HfC exhibits a relatively lower oxygen partial pressure for the initiation of oxidation compared to TiC at 2500 °C, suggesting that HfC might be preferentially oxidized. Similar preferential oxidation laws have been reported in recent studies [28,38,39,52]. TiC and HfC exist as (Hf, Ti)C single-phase solid solutions with a homogeneous distribution of elements (Fig. 1). Consequently, the preferential oxidation of Hf and the delayed oxidation of Ti dominate the structural evolution during the initial oxidation stage.

A region of coexistence between the carbides and their corresponding oxides is observed in the HfC and TiC volatility diagrams. Despite the lack of thermodynamic data for oxycarbides, it is reasonable to infer that this coexistence region is associated with the incompletely oxidized transition phases, as supported by characterization results (Figs. 4–5). Previous studies have reported a two-stage oxidation process for binary carbides such as HfC and ZrC [53–56]. In the first stage, HfC/ZrC is oxidized by trace amounts of oxygen, forming HfC_xO_y/ZrC_xO_y oxycarbides and carbon precipitation. In the second stage, the oxycarbides and carbon further oxidize, leading to the formation of HfO_2/ZrO_2 along with the release of CO/CO_2.

In this study, (Hf, Ti)C_xO_y phases (Phase a), (Ti, Hf)C_xO_y-L (Phase c), (Ti, Hf)C_xO_y-H (Phase e), and carbon were detected in HT1-HT3 after oxidation. Moreover, it can be inferred that all samples undergo a similar oxidation process, forming these transition products. Similar oxycarbides have been observed in the oxidation processes of (Zr, Ti)C [18], (Zr, Hf, Ti)C [28,57] and (Hf, Ta, Zr, Nb)C [31]. However, most reported oxycarbides are amorphous, whereas the (Hf, Ti)C_xO_y phase detected in our study retains the FCC structure of the (Hf, Ti)C matrix. The ultra-high temperature of 2500 °C facilitates the crystallization of the oxycarbides, which provides valuable microstructural information for our investigation.

Based on the above-mentioned thermodynamic investigations and experimental characterization results, the total oxidation process of (Hf, Ti)C can be described by equations (6)–(12):

$$(Hf, Ti)C_{(s)} + O_{2(g)} \rightarrow (Hf, Ti)C_xO_{y(s)} + C_{(s)} \quad (6)$$

$$(Hf, Ti)C_xO_{y(s)} + O_{2(g)} \rightarrow (Ti, Hf)C_xO_y - L_{(s)} + HfO_{2(s)} + C_{(s)} \quad (7)$$

$$(Ti, Hf)C_xO_y - L_{(s)} + O_{2(g)} \rightarrow (Ti, Hf)C_xO_y - H_{(s)} + HfO_{2(s)} \quad (8)$$

$$(Ti, Hf)C_xO_y - H_{(s)} + O_{2(g)} \rightarrow TiO_{(l)} + CO_{(g)} \quad (9)$$

$$TiO_{(l)} + O_{2(g)} \rightarrow TiO_{2(l)} \quad (10)$$

$$C_{(s)} + O_{2(g)} \rightarrow CO_{(g)} \quad (11)$$

$$CO_{(g)} + O_{2(g)} \rightarrow CO_{2(g)} \quad (12)$$

Fig. 6 depicts the schematic diagram of the oxidation mechanism of (Hf, Ti)C at 2500 °C. During the initial stage of oxidation under deficient oxygen partial pressures (Fig. 6a–b), oxygen dissolve into the (Hf, Ti)C lattice, replacing C atoms and generating the (Hf, Ti)C_xO_y transition phase, accompanied by the precipitation of carbon. With the ongoing diffusion of oxygen from the surface towards the transition layer, the concentration of dissolved oxygen in the (Hf, Ti)C_xO_y lattice gradually increases. As depicted in Fig. 6c, when the oxygen concentration in the lattice reaches a certain level, Hf atoms preferentially react with oxygen, forming HfO_2. The small (Ti, Hf)C_xO_y-L phases remain, retaining the FCC structure. Consequently, the transitional region exhibits a complex structure comprising (Hf, Ti)C_xO_y, HfO_2, (Ti, Hf)C_xO_y-L and C.

With the progression of oxidation, Hf atoms within the (Hf, Ti)C_xO_y phase progressively diffuse outward, forming HfO_2. Additionally, with the ongoing diffusion of O atoms from the external environment towards the interior, Hf and O atoms within the (Ti, Hf)C_xO_y-L phase combine to form HfO_2. This process leads to a continuous decrease in Hf content and a simultaneous rise in O content within the (Ti, Hf)C_xO_y-L phase, ultimately giving rise to the formation of the (Ti, Hf)C_xO_y-H phase (Fig. 6d). Through the process mentioned above, the initial transition layer gradually transforms into the major structure of the oxide layer consisting of HfO_2 and (Ti, Hf)C_xO_y-H.

With prolonged oxidation time, the residual (Ti, Hf)C_xO_y-H phase undergoes complete oxidation, resulting in the formation of TiO_2/TiO and the release of CO_2/CO (Fig. 6e). The TiO_2/TiO in the outermost layer experience severe evaporation due to extremely high temperatures. Consequently, only a continuous and firm HfO_2 frame (Layer I) remains (Fig. 6f).

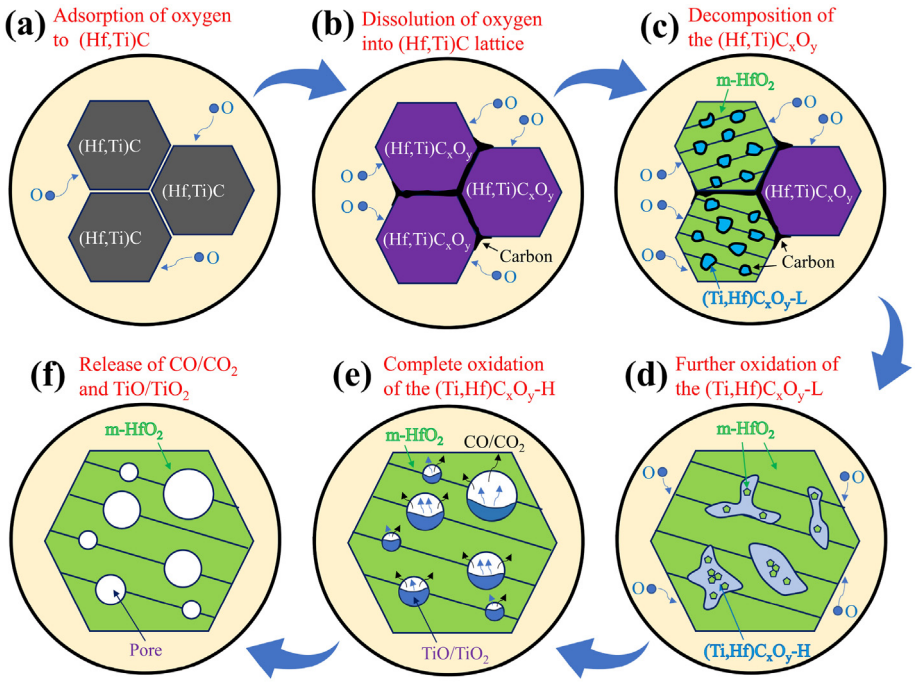

Fig. 6. Schematic diagram of (Hf, Ti)C oxidation mechanism. (a) Adsorption of oxygen to (Hf, Ti)C surface; (b) Dissolution of oxygen into (Hf, Ti)C lattice to form (Hf, Ti)C_xO_y; (c) Decomposition of (Hf, Ti)C_xO_y into (Ti, Hf)C_xO_y-L; (d) Oxidation of Ti, Hf)C_xO_y-L to (Ti, Hf)C_xO_y-H and HfO_2; (e) Complete oxidation of (Ti, Hf)C_xO_y-H; (f) Release of gaseous products and formation of pores.

2.5. *Effect of Ti content on the oxidation resistance of (Hf, Ti)C*

Table 1 shows the reaction rate constants k change for Stage I (k_1) and Stage II (k_2) as the Ti content increases, indicating the influence of Ti content on the oxidation kinetics of (Hf, Ti)C. This influence can be attributed to the effect of Ti on the microstructural evolution of the oxide layer. On the one hand, the Ti content determines the proportion of (Ti, Hf)C_xO_y-H phase within the major structure of the oxide layer (HfO_2 + (Ti, Hf)C_xO_y-H). Fig. S8 shows the details of the oxide layer's major structure in (Hf, Ti)C after oxidation at 2500 °C for 300 s and 2000 s. Figs. S8a–c demonstrate a notable increase in the number of (Ti, Hf)C_xO_y-H particles within HfO_2 as the Ti content rises. On the other hand, the Ti content impacts the diffusion coefficient of carbon within the (Hf, Ti)C lattice. The diffusion coefficients (D) of carbon in HfC and TiC can be determined using Equation (13) [58], which follows the Arrhenius behavior:

$$D = D_0\, exp(-Q/RT) \tag{13}$$

where D_0 denotes the preexponential factor, Q is the activation energy, R is the gas constant, and T refers to the testing temperature. The values of D_0 and Q for carbon in HfC and TiC, as provided in the study by Wallace [58], are presented in Table S1. Fig. S9 displays the calculated values of D using Equation (14) within the relevant temperature range. It is noteworthy that D of carbon in TiC is two orders of magnitude higher than that in HfC at 2500 °C. Consequently, adding Ti increases the diffusion rate of carbon in HfC, which is similar to the phenomenon observed in the Zr–Ti–C [18] and Zr–U–C [58] systems.

In Stage I, the reaction rate constant k_1 initially increases and then decreases as the Ti content rises. In the initial oxidation stage (<900 s), oxygen diffusion within the oxide layer primarily controls the oxidation rate. The addition of Ti enhances the diffusion of carbon in (Hf, Ti)C, promoting the precipitation of carbon. The precipitated carbon undergoes oxidation, producing CO/CO_2 gas and escaping, creating rapid pathways for the inward diffusion of oxygen. Thus, as Ti increases, k_1 first rises.

Nevertheless, as demonstrated in Figs. S8d–f, an increase in Ti content also leads to a higher proportion of residual (Ti, Hf)C_xO_y-H within the major structure of the oxide layer (HfO_2 + (Ti, Hf)C_xO_y-H). The HfO_2/(Ti, Hf)C_xO_y-H interface represents a coherent phase boundary (Fig. 5). The coherent boundary with elemental mixing and lattice distortion served as an effective diffusion barrier, impeding the inward diffusion of oxygen. This phenomenon is similar to the sluggish diffusion effect observed in high entropy carbides (HECs) [49–51]. Consequently, when the Ti content reaches a certain threshold, k_1 decreases.

In Stage II, the reaction rate constant k_2 exhibits an initial decrease followed by an increase with growing Ti content. This behavior can be attributed to the rapid thickening of the oxide layer during oxidation, where the structural integrity of the oxide layer gradually becomes crucial for oxidation resistance. The oxidation of HfC to produce HfO_2 involves volume expansion, leading to the interface mismatch, stress concentration as well as formation of a porous oxide layer [59]. The incorporation of Ti introduces low-melting Ti-containing oxides (e.g., TiO_2) during the oxidation of (Hf, Ti)C. These oxides can fill the pores and hinder the inward diffusion of oxygen [60]. Furthermore, evaporation of Ti-containing oxides at elevated temperatures creates space for accommodating the volume expansion from HfO_2 formation, thereby reducing defects generation, relaxing interface mismatch, and releasing stress concentration. As a result, an increase in Ti content leads to a decline in the number of pores within the oxide layer, contributing to a decrease in k_2. However, at excessively high Ti contents, the intense evaporation of low-melting Ti-containing oxides can lead to the formation of numerous pores, leading to a decline in oxidation resistance (Fig. S8f). Consequently, when the Ti content reaches a specific threshold, k_2 exhibits an increase instead.

In conclusion, the oxidation resistance of (Hf, Ti)C is influenced by various competing factors associated with the Ti content. During the initial stage of oxidation, HT1 demonstrates the lowest oxidation rate. Conversely, although HT2 exhibits a faster oxidation rate during the early stages of oxidation, it forms a more extensive and stable oxide layer over time, offering enhanced protection. Therefore, HT1 exhibits superior initial oxidation resistance, whereas HT2 demonstrates the best long-term oxidation resistance.

3. Conclusion

The static oxidation behavior of (Hf, Ti)C solid solutions was investigated in air at 2500 °C under an oxygen partial pressure of 4.2 kPa. The microstructural evolution was systematically examined after oxidation for 300–2000 s. Results show that the Ti substitutions can reduce the oxidation rate and improve the oxidation resistance of pure HfC significantly. For example, the oxide layer thickness of HT2 is reduced by 62.29 % compared to pure HfC after oxidation at 2500 °C for 2000 s. The oxidation kinetics of (Hf, Ti)C follow a two-stage parabolic law. The calculated volatility diagrams indicate a preferential oxidation tendency of Hf. As for (Hf, Ti)C, it is firstly oxidized to (Hf, Ti)C_xO_y (Hf-rich oxycarbide), which subsequently decomposes to HfO_2, (Ti, Hf)C_xO_y-L (Ti-rich oxycarbide with low O content), and carbon. Then (Ti, Hf)C_xO_y-L further transforms into (Ti, Hf)C_xO_y-H (Ti-rich oxycarbide with higher O content) and disperses within HfO_2, which finally constitutes the major structure of the oxide layer. Notably, the (Ti, Hf)C_xO_y-H is coherently related with the surrounding HfO_2 along (111) crystal plane direction, causing lattice distortion and impeding the inward diffusion of oxygen. The Ti content affects the diffusion of carbon in (Hf, Ti)C lattice and the distribution of Ti-rich oxycarbide, which will further determine the structural integrity of the oxide layer. Specifically, among all the candidates in this paper, HT2 was demonstrated to be the best long-term oxidation resistance.

4. Materials and methods

4.1. Material preparation

Commercial HfC (99 %, 1–3 μm, Macklin Biochemical, China) and TiC (99.5 %, 1–3 μm, Macklin Biochemical, China) powders were employed as raw materials. Four compositions (HT0, HT1, HT2, and HT3) were designed based on 0 at%, 10 at%, 20 at%, and 30 at% Ti content to investigate the effect of Ti contents on the oxidation resistance, respectively. The initial powders were weighed according to the corresponding molar ratio and mixed by planetary ball milling with stirring at 150 rpm for 6 h. Ethanol, ZrO_2 balls, and pots were selected as the ball milling media. The ball-to-powder mass ratio was set to 5:1. The powder mixtures were dried in an oven at 40 °C for 30 h after milling. Subsequently, the powder mixtures were sintered inside graphite dies using a hot-pressing sintering furnace (ZT-40-21Y, Shanghai Chenhua Technology, China) at 1900 °C in a vacuum. The samples were held at a vertical pressure of 30 MPa for 1 h with a heating rate of 10 °C/min. The schematic of the preparation process is illustrated in Fig. S10. Ceramic blocks with a diameter of 60 mm and a thickness of 10 mm are obtained after hot pressing sintering. Sintered ceramics were cut into small disks with a diameter of 15 mm and a thickness of 2 mm for the next oxidation test. The surfaces were well polished and then ultrasonic cleaned in ethanol.

4.2. Oxidation test

High-temperature oxidation tests of HT0-HT3 were performed using a specially designed oxidation apparatus. The schematic of the oxidation apparatus is shown in Fig. S11. The samples were positioned on a graphite heater at the center of the induction coil. Only the bottom of the sample was in contact with the graphite heater. The samples were then heated to 2500 °C in a vacuum by adjusting the power of the high-frequency induction power supply. The temperature of the sample surface was monitored using a two-color infrared pyrometer (Marathon MR1SCSF, Raytek, America, accuracy: ± (0.5 % T_{meas} + 2 °C)). The average heating rate of the samples was 15 °C/s. After reaching the desired temperature, flowing dry air was introduced into the system. The pressure inside the chamber was regulated at 20 kPa (pO_2=4.2 kPa) using a pressure control unit (ZCMD-I-10-LED, Chengdu Zhenghua Electronic Instruments, China, applicable range: 1×10^2 Pa–2×10^4 Pa). When the pressure was stabilized, the holding time was set at 300, 600, 900, 1500 and 2000 s, respectively. The oxidized samples were labeled according to the oxidation time, such as HT1-300. Upon reaching the specified time, the heating was stopped, and the sample was cooled in the furnace under vacuum conditions with the support of a cooling system. The samples were rapidly cooled from 2500 °C to room temperature in approximately 10 min.

4.3. Characterizations

The phase composition of the specimens before and after oxidation was determined by an X-ray diffraction (XRD) analyzer (D/max-2550VB, Rigaku Co., Japan) with CuKα radiation at a scanning rate of 2°/min. The Rietveld refinements on the XRD patterns were carried out using the general structure analysis system software (GSAS-II) [61]. The actual densities and open porosities of all samples were measured by the Archimedes method. The theoretical densities of (Hf, Ti)C bulks were determined from XRD refinement results, as shown in Table S2. The relative density of HT0, HT1, HT2 and HT3 is 96.20 %, 97.68 %, 95.09 % and 95.07 %, respectively. Electron probe microanalysis (EPMA, Jxa8230, JEOL, Japan) was utilized to determine the distribution of the elements in the samples. Micromorphology was observed by a scanning electron microscope (SEM, MIRA4 LMH, TESCAN, Czech) equipped with an energy dispersive spectroscope (EDS, Ultim Max 40, Oxford Instruments, UK). At least five locations in the center of the cross-section were selected to measure the average thickness of the oxide layer using SEM. Nanoscale characterizations were achieved by scanning/-transmission electron microscopy (S/TEM, Talos F200x, FEI, Netherlands) coupled with an EDS system. Cross-sectional TEM samples were prepared by a focused ion beam (FIB, Helios 5UC, Thermo Fisher Scientific, America) using the in-situ lift-out technique. The thermodynamic data required for constructing the Ellingham diagram for the Hf–Ti–C–O system were obtained from the HSC Chemistry software. Volatility diagrams were calculated based on the FactPS and FToxid databases in FactSage.

CRediT authorship contribution statement

Shiyan Chen: Investigation, Data curation, Writing – original draft, Validation. **Zhaoke Chen:** Writing – review & editing, Methodology, Project administration. **Jinming Wang:** Resources, Conceptualization. **Yi Zeng:** Conceptualization, Writing – review & editing. **Weilong Song:** Validation, Data curation. **Xiang Xiong:** Project administration, Supervision. **Xingchao Li:** Resources, Supervision. **Tongqi Li:** Resources, Supervision. **Yichen Wang:** Writing – review & editing.

Declaration of competing interest

The authors declare that they have no known competing financial interests or personal relationships that could have appeared to influence the work reported in this paper.

Acknowledgements

This work was supported by the National Natural Science Foundation of China grant numbers [52072410].

Appendix A. Supplementary data

Supplementary data to this article can be found online at https://doi.org/10.1016/j.apmate.2023.100168.

References

[1] W.G. Fahrenholtz, G.E. Hilmas, I.G. Talmy, J.A. Zaykoski, Refractory diborides of zirconium and hafnium, J. Am. Ceram. Soc. 90 (2007) 1347–1364.

[2] M.M. Opeka, I.G. Talmy, E.J. Wuchina, J.A. Zaykoski, S.J. Causey, Mechanical, thermal, and oxidation properties of refractory hafnium and zirconium compounds, J. Eur. Ceram. Soc. 19 (1999) 2405–2414.

[3] W.G. Fahrenholtz, E.J. Wuchina, W.E. Lee, Y.C. Zhou, Ultra-High Temperature Ceramics: Materials for Extreme Environment Applications, first ed., Wiley, Hoboken, 2014.

[4] W.G. Fahrenholtz, G.E. Hilmas, Ultra-high temperature ceramics: Materials for extreme environments, Scripta Mater. 129 (2017) 94–99.

[5] J. Binner, M. Porter, B. Baker, J. Zou, V. Venkatachalam, V.R. Diaz, A. D'Angio, P. Ramanujam, T. Zhang, T.S.R.C. Murthy, Selection, processing, properties and applications of ultra-high temperature ceramic matrix composites, UHTCMCs — A review, Int. Mater. Rev. 65 (2019) 389–444.

[6] M.D. Tong, Q.G. Fu, L. Zhou, T. Feng, H.J. Li, T. Li, K. Li, Ablation behavior of a novel HfC-SiC gradient coating fabricated by a facile one-step chemical vapor co-deposition, J. Eur. Ceram. Soc. 38 (2018) 4346–4355.

[7] T. Glechner, O.E. Hudak, T. Wojcik, L. Haager, F. Bohrn, H. Hutter, O. Hunold, J. Ramm, S. Kolozsvári, E. Pitthan, Influence of the non-metal species on the oxidation kinetics of Hf, HfN, HfC, and HfB_2 coatings, Mater. Des. 211 (2021) 110136.

[8] S. Shimada, K. Nakajima, M. Inagaki, Oxidation of single crystals of hafnium carbide in a temperature range of 600° to 900° 3C, J. Am. Ceram. Soc. 80 (1997) 1749–1756.

[9] J.A. Scott, X.Q. He, D.W. Lipke, The role of microstructure on high-temperature oxidation behavior of hafnium carbide, J. Am. Ceram. Soc. 106 (2023) 3116–3126.

[10] C.B. Bargeron, R.C. Benson, A.N. Jette, T.E. Phillips, Oxidation of hafnium carbide in the temperature range 1400 to 2060 °C, J. Am. Ceram. Soc. 76 (1993) 1040–1046.

[11] J.B. Berkowitz-Mattuck, High-temperature oxidation: IV. zirconium and hafnium carbides, J. Electrochem. Soc. 114 (1967) 1030–1033.

[12] P. Makurunje, I. Sigalas, J. Binner, Scale characterisation of an oxidised (Hf, Ti)C-SiC ultra-high temperature ceramic matrix composite, J. Eur. Ceram. Soc. 41 (2021) 167–175.

[13] Y.Q. Tan, C. Chen, S.G. Li, X.C. Han, J.X. Xue, T. Liu, X.S. Zhou, H.B. Zhang, Oxidation behaviours of high-entropy transition metal carbides in 1200 °C water vapor, J. Alloys Compd. 816 (2020) 152523.

[14] K.A. Kane, B.A. Pint, D. Mitchell, J.A. Haynes, Oxidation of ultrahigh temperature ceramics: kinetics, mechanisms, and applications, J. Eur. Ceram. Soc. 41 (2021) 6130–6150.

[15] S. Vorotilo, K. Sidnov, I.Y. Mosyagin, A.V. Khvan, E.A. Levashov, E.I. Patsera, I.A. Abrikosov, Ab-initio modeling and experimental investigation of properties of ultra-high temperature solid solutions $Ta_xZr_{1-x}C$, J. Alloys Compd. 778 (2019) 480–486.

[16] V.V. Kurbatkina, E.I. Patsera, E.A. Levashov, S. Vorotilo, SHS processing and cconsolidation of Ta–Ti–C, Ta–Zr–C, and Ta–Hf–C carbides for ultra-high-temperatures application, Adv. Eng. Mater. 20 (2018) 1701075.

[17] J. Zhang, S. Wang, W. Li, Y.P. Yu, J.M. Jiang, Understanding the oxidation behavior of Ta–Hf–C ternary ceramics at high temperature, Corrosion Sci. 164 (2020) 108348.

[18] H.L. Lun, J.H. Yuan, Y. Zeng, X. Xiong, Q. Wang, Z.M. Ye, Mechanisms responsible for enhancing low-temperature oxidation resistance of nonstoichiometric (Zr, Ti)C, J. Am. Ceram. Soc. 105 (2022) 5309–5324.

[19] L. Backman, E.J. Opila, Thermodynamic assessment of the group IV, V and VI oxides for the design of oxidation resistant multi-principal component materials, J. Eur. Ceram. Soc. 39 (2019) 1796–1802.

[20] Y.X. Xu, X.H. Pan, S.S. Huang, X.T. Xu, Y.R. Niu, X. Zhong, X.B. Zheng, Effect of solid oxidation products on the ablation mechanisms of ZrC and HfC based coatings above 2000 °C, J. Mater. Res. Technol. 22 (2023) 1900–1910.

[21] J.C. Ren, Y.L. Zhang, P.F. Zhang, T. Li, J.H. Li, Y. Yang, Ablation resistance of HfC coating reinforced by HfC nanowires in cyclic ablation environment, J. Eur. Ceram. Soc. 37 (2017) 2759–2768.

[22] J. Zhang, Y.L. Zhang, R.C. Chen, X.F. Zhu, Y.Q. Fu, Effect of microstructure on the ablation behavior and mechanical properties of CVD-HfC coating, Corrosion Sci. 192 (2021) 109815.

[23] D. Zhao, C.R. Zhang, H.F. Hu, Y.D. Zhang, Ablation behavior and mechanism of 3D C/ZrC composite in oxyacetylene torch environment, Compos. Sci. Technol. 71 (2011) 1392–1396.

[24] B.H. Zhang, J. Yin, J.Q. Zheng, X.J. Liu, Z.R. Huang, J. Dusza, D.L. Jiang, High temperature ablation behavior of pressureless sintered Ta0.8Hf0.2C-based ultra-high temperature ceramics, J. Eur. Ceram. Soc. 40 (2020) 1784–1789.

[25] Y.C. Wang, B.H. Zhang, C.Y. Zhang, J. Yin, M.J. Reece, Ablation behaviour of (Hf–Ta–Zr–Nb)C high entropy carbide ceramic at temperatures above 2100 °C, J. Mater. Sci. Technol. 113 (2022) 40–47.

[26] Y.C. Wang, D. Yu, J. Yin, B.H. Zhang, H.F. Zhang, X.J. Liu, Y.L. An, M.J. Reece, Z.R. Huang, Ablation behavior of (Hf–Ta–Zr–Nb–Ti) C high-entropy carbide and (Hf–Ta–Zr–Nb–Ti) C–*x*SiC composites, J. Am. Ceram. Soc. 105 (2022) 6395–6406.

[27] S.Y. Chen, Y. Zeng, X. Xiong, H.L. Lun, Z.M. Ye, T.X. Jiang, L.W. Yang, J. Zhang, L.P. Liu, G.L. Wang, J. Li, X.Q. Xie, C.H. Yan, Static and dynamic oxidation behaviour of silicon carbide at high temperature, J. Eur. Ceram. Soc. 41 (2021) 5445–5456.

[28] H.L. Lun, Y. Zeng, X. Xiong, Z.M. Ye, Z.W. Zhang, X.C. Li, H.K. Chen, Y.F. Liu, Oxidation behavior of non-stoichiometric (Zr, Hf, Ti)C_x carbide solid solution powders in air, J. Adv. Ceram. 10 (2021) 741–757.

[29] L.F. He, J.J. Li, H.Q. Nian, X.H. Wang, Y.W. Bao, M.S. Li, J.Y. Wang, Y.C. Zhou, Oxidation behavior of ternary carbide ceramics in Hf–Al–C System in Air, J. Am. Ceram. Soc. 93 (2010) 3427–3431.

[30] L. Backman, J. Gild, J. Luo, E.J. Opila, Part II: Experimental verification of computationally predicted preferential oxidation of refractory high entropy ultra-high temperature ceramics, Acta Mater. 197 (2020) 81–90.

[31] Y.C. Wang, R.Z. Zhang, B.H. Zhang, O. Skurikhina, P. Balaz, V. Araullo-Peters, M.J. Reece, The role of multi-elements and interlayer on the oxidation behaviour of (Hf–Ta–Zr–Nb)C high entropy ceramics, Corrosion Sci. 176 (2020) 109019.

[32] H.X. Wang, S.Y. Wang, Y.J. Cao, W. Liu, Y.G. Wang, Oxidation behaviors of $(Hf_{0.25}Zr_{0.25}Ta_{0.25}Nb_{0.25})C$ and $(Hf_{0.25}Zr_{0.25}Ta_{0.25}Nb_{0.25})C$-SiC at 1300–1500 °C, J. Mater. Sci. Technol. 60 (2021) 147–155.

[33] M.M. Opeka, I.G. Talmy, J. Zaykoski, Oxidation-based materials selection for 2000°C + hypersonic aerosurfaces: Theoretical considerations and historical experience, J. Mater. Sci. 39 (2004) 5887–5904.

[34] Q. Wen, Z. Yu, R. Riedel, E. Ionescu, Significant improvement of high-temperature oxidation resistance of HfC/SiC ceramic nanocomposites with the incorporation of a small amount of boron, J. Eur. Ceram. Soc. 40 (2020) 3499–3508.

[35] A. Gaydaychuk, S. Linnik, A. Mitulinsky, S. Zenkin, Effect of Al addition on the oxidation resistance of HfC thin films, Coatings 12 (2021) 27.

[36] L. Pienti, L. Silvestroni, E. Landi, C. Melandri, D. Sciti, Microstructure, mechanical properties and oxidation behavior of TaC- and HfC-based materials containing short SiC fiber, Ceram. Int. 41 (2015) 1367–1377.

[37] Z.M. Ye, Y. Zeng, X. Xiong, Q.B. Wen, H.L. Lun, Elucidating the role of preferential oxidation during ablation: Insights on the design and optimization of multicomponent ultra-high temperature ceramics, J. Adv. Ceram. 11 (2022) 1956–1975.

[38] D.M. Van Wie, D.G. Drewry Jr., D.E. King, C.M. Hudson, The hypersonic Environment: required operating conditions and design challenges, J. Mater. Sci. 39 (2004) 5915–5924.

[39] D.W. Ni, Y. Cheng, J.P. Zhang, J.X. Liu, J. Zou, B.W. Chen, H.Y. Wu, H.J. Li, S.M. Dong, J.C. Han, X.H. Zhang, Q.G. Fu, G.J. Zhang, Advances in ultra-high temperature ceramics, composites, and coatings, J. Adv. Ceram. 11 (2021) 1–56.

[40] S.F. Tang, C.L. Hu, Design, preparation and properties of carbon fiber reinforced ultra-high temperature ceramic composites for aerospace applications: A review, J. Mater. Sci. Technol. 33 (2017) 117–130.

[41] J.C. Slater, Atomic radii in crystals, J. Chem. Phys. 41 (1964) 3199–3204.

[42] M. Zhang, D. Yao, X. Wang, L. Deng, Air oxidation of a $Zr_{55}Cu_{30}Al_{10}Ni_5$ bulk metallic glass at its super cooled liquid state, Corrosion Sci. 82 (2014) 410–419.

[43] S. Taniguchi, T. Shibata, A. Okada, Oxidation behavior of $TiN_{0.74}$ at high temperatures, Mater. Trans., JIM 30 (1989) 765–771.

[44] V. Presser, A. Loges, Y. Hemberger, K.G. Nickel, Microstructural evolution of silica on single-crystal silicon carbide. Part I: Devitrification and oxidation rates, J. Am. Ceram. Soc. 92 (2009) 724–731.

[45] A.M. Alper, High temperature oxides. Part II. Oxides of rare Earth, in: Titanium, Zirconium, Hafnium, NNiobium, and Tantalum, first ed., Academic Press, New York, 1970.

[46] X.H. Pan, Y.R. Niu, X.T. Xu, X. Zhong, M.H. Shi, X.B. Zheng, C.X. Ding, Long time ablation behaviors of designed ZrC-SiC-TiC ternary coatings for environments above 2000 °C, Corrosion Sci. 170 (2020) 108645.

[47] A. Bronson, J. Chessa, An evaluation of vaporizing rates of SiO_2 and TiO_2 as protective coatings for ultrahigh temperature ceramic composites, J. Am. Ceram. Soc. 91 (2008) 1448–1452.

[48] K. Constant, R. Kieffer, P. Ettmayer, Über das pseudoternäre system "HfO"-HfN-HfC, Monatsh. Chem. 106 (1975) 973–981.

[49] C. Oses, C. Toher, S. Curtarolo, High-entropy ceramics, Nat. Rev. Mater. 5 (2020) 295–309.

[50] J.Y. Zhou, J.Y. Zhang, F. Zhang, B. Niu, L.W. Lei, W.M. Wang, High-entropy carbide: A novel class of multicomponent ceramics, Ceram. Int. 44 (2018) 22014–22018.

[51] H.M. Xiang, Y. Xing, F.Z. Dai, H.J. Wang, L. Su, L. Miao, G.J. Zhang, Y.G. Wang, X.W. Qi, L. Yao, H.L. Wang, B. Zhao, J.Q. Li, Y.C. Zhou, High-entropy ceramics: Present status, challenges, and a look forward, J. Adv. Ceram. 10 (2021) 385–441.

[52] L. Backman, J. Gild, J. Luo, E.J. Opila, Part I: Theoretical predictions of preferential oxidation in refractory high entropy materials, Acta Mater. 197 (2020) 20–27.

[53] F. Réjasse, O. Rapaud, G. Trolliard, O. Masson, A. Maître, Experimental investigation and thermodynamic evaluation of the C–Hf–O ternary system, J. Am. Ceram. Soc. 100 (2017) 3757–3770.

[54] X.P. Li, W.T. Hu, Superfluous oxygen diffusion induced amorphization of $ZrC_{0.6}O_{0.4}$ and transformation of amorphous layer under electron beam irradiation, J. Mater. Res. 31 (2016) 137–147.

[55] S. Shimada, M. Inagaki, K. Matsui, Oxidation kinetics of hafnium carbide in the temperature range of 480 °C to 600 °C, J. Am. Ceram. Soc. 75 (1992) 2671–2678.

[56] G.R. Rao, V. Venugopal, Kinetics and mechanism of the oxidation of ZrC, J. Alloys Compd. 206 (1994) 237–242.

[57] Z.M. Ye, Y. Zeng, X. Xiong, T.X. Qian, H.L. Lun, Y.L. Wang, W. Sun, Z.K. Chen, L.J. Zhang, P. Xiao, New insight into the formation and oxygen barrier mechanism of carbonaceous oxide interlayer in a multicomponent carbide, J. Am. Ceram. Soc. 103 (2020) 6978–6990.

[58] T. Wallace Sr, D. Butt, Review of diffusion and vaporization of group 4 and 5 transition metal carbides, in: S.T. Oyama (Ed.), The Chemistry of Transition Metal Carbides and Nitrides, Springer, Berlin, 1996, pp. 53–90.

[59] T. Glechner, O.E. Hudak, T. Wojcik, L. Haager, F. Bohrn, H. Hutter, O. Hunold, J. Ramm, S. Kolozsvári, E. Pitthan, D. Primetzhofer, H. Riedl, Influence of the non-

metal species on the oxidation kinetics of Hf, HfN, HfC, and HfB_2 coatings, Mater. Des. 211 (2021) 110136.
[60] Y. Zeng, D.N. Wang, X. Xiong, X. Zhang, P.J. Withers, W. Sun, M. Smith, M.W. Bai, P. Xiao, Ablation-resistant carbide $Zr_{0.8}Ti_{0.2}C_{0.74}B_{0.26}$ for oxidizing environments up to 3,000 °C, Nat. Commun. 8 (2017) 15836.
[61] B.H. Toby, R.B.V. Dreele, GSAS-II: The genesis of a modern open-source all purpose crystallography software package, J. Appl. Crystallogr. 46 (2013) 544–549.

Shiyan Chen is a doctoral candidate in the State Key Laboratory of Powder Metallurgy at Central South University. His current research is focused on the development of ultra-high temperature structural ceramics, with a particular emphasis on their oxidation and ablation resistance.

Zhaoke Chen is a professor and a doctoral supervisor in the State Key Laboratory of Powder Metallurgy at Central South University. His main research interests include preparation, structural design and control of ultra-high temperature ceramic modified C/C composites, neutron irradiation resistant SiC_f/SiC composites, ultra-high temperature ceramic coating materials.

Xiong Xiang is a professor and a doctoral supervisor in Central South University, and a Distinguished Professor of Changjiang Scholars. He has long been engaged in aerospace new materials research and application development, with a focus on C/C composite materials, ultra-high temperature ceramic composite materials, powder metallurgy materials and other novel materials preparation technologies.